Chinese Chemical Letters 36 (2025) 109568

Contents lists available at ScienceDirect

Chinese Chemical Letters

journal homepage: www.elsevier.com/locate/cclet

Al-F co-doping towards enhanced electrolyte-electrodes interface properties for halide and sulfide solid electrolytes

Han Yan[a,b], Jingming Yao[b], Zhangran Ye[b], Qiaoquan Lin[a], Ziqi Zhang[b], Shulin Li[b], Dawei Song[c], Zhenyu Wang[d,*], Chuang Yu[e,*], Long Zhang[a,b,*]

[a] College of Physics and Energy, Fujian Normal University, Fuzhou 350117, China
[b] Clean Nano Energy Center, State Key Laboratory of Metastable Materials Science and Technology, Yanshan University, Qinhuangdao 066004, China
[c] Tianjin Key Laboratory for Photoelectric Materials and Devices, School of Materials Science and Engineering, Tianjin University of Technology, Tianjin 300384, China
[d] Guilin Electrical Equipment Scientific Research Institute Co., Ltd., Guilin 541004, China
[e] State Key Laboratory of Advanced Electromagnetic Engineering and Technology, School of Electrical and Electronic Engineering, Huazhong University of Science and Technology, Wuhan 430000, China

ARTICLE INFO

Article history:
Received 6 December 2023
Revised 18 January 2024
Accepted 23 January 2024
Available online 1 February 2024

Keywords:
Solid electrolytes
Li halides
Li_2ZrCl_6
Li argyrodites
Fluorine doping

ABSTRACT

All-solid-state Li batteries (ASSLBs) using solid electrolytes (SEs) have gained significant attention in recent years considering the safety issue and their high energy density. Despite these advantages, the commercialization of ASSLBs still faces challenges regarding the electrolyte/electrodes interfaces and growth of Li dendrites. Elemental doping is an effective and direct method to enhance the performance of SEs. Here, we report an Al-F co-doping strategy to improve the overall properties including ion conductivity, high voltage stability, and cathode and anode compatibility. Particularly, the Al-F co-doping enables the formation of a thin Li-Al alloy layer and fluoride interphases, thereby constructing a relatively stable interface and promoting uniform Li deposition. The similar merits of Al-F co-doping are also revealed in the Li-argyrodite series. ASSLBs assembled with these optimized electrolytes gain good electrochemical performance, demonstrating the universality of Al-F co-doping towards advanced SEs.

© 2024 Published by Elsevier B.V. on behalf of Chinese Chemical Society and Institute of Materia Medica, Chinese Academy of Medical Sciences.

Li-ion batteries have been widely used in portable electronic devices. However, concerns have arisen regarding their energy density limitations and the potential safety risks associated with flammable organic liquid electrolytes [1–3]. All-solid-state Li batteries (ASSLBs) are expected to replace flammable liquid electrolytes in traditional Li-ion batteries, thereby addressing the safety issues. Moreover, ASSLBs allow the use of high-voltage cathodes and Li metal anodes, enabling to achieve a higher energy density. The selection and use of solid electrolytes (SEs) are thus playing a critical role towards high performance ASSLBs [4,5].

In recent years, diverse SEs have been developed. Among them, halides exhibit relatively high ionic conductivity, good deformability, and high voltage stability, making them a promising class of SEs similar to sulfide-based SEs. Typically, as an important member of the halide SE family, Li_2ZrCl_6 (LZC) has attracted widespread research interests due to its low cost and high abundance of Zr element in the Earth's crust (estimated raw material cost of $5.95 USD/kg) [6,7]. However, the poor stability against Li metal hinders its practical applications. The thermodynamic electrochemical window of Li-M-X (M is the metal cation in the highest covalent state) ternary chlorides, calculated theoretically, indicates their instability against metallic Li electrode [8–11]. The instability at the anode interface can lead to short-circuits and a sharp increase in interface resistance [12]. Moreover, Cl-based halides can still be oxidized at high oxidation potentials and thus degrade the battery cycling performance [13–15]. Therefore, it is crucial for LZC to improve the ionic conductivity, stability against Li metal, and high-voltage stability.

The SE properties have been enhanced through regulating the preparation technique, elemental doping, using composite materials, and so on [16,17]. Elemental doping has been proven an effective method to enhance the properties of SEs [18–21]. Previous studies revealed that cation doping can increase the vacancy concentration in the lattice and widen the Li^+ diffusion channels, thereby achieving higher ionic conductivity [22,23]. Wu *et al.* reported that LLZO can be optimized by doping method in six different ways including: pellet density, phase structure, ion occupancy behaviors, Li-ion content, vacancy concentration, and local

* Corresponding authors.
E-mail addresses: wzy2012bg@163.com (Z. Wang), cyu2020@hust.edu.cn (C. Yu), longzhang2023@163.com (L. Zhang).

https://doi.org/10.1016/j.cclet.2024.109568
1001-8417/© 2024 Published by Elsevier B.V. on behalf of Chinese Chemical Society and Institute of Materia Medica, Chinese Academy of Medical Sciences.

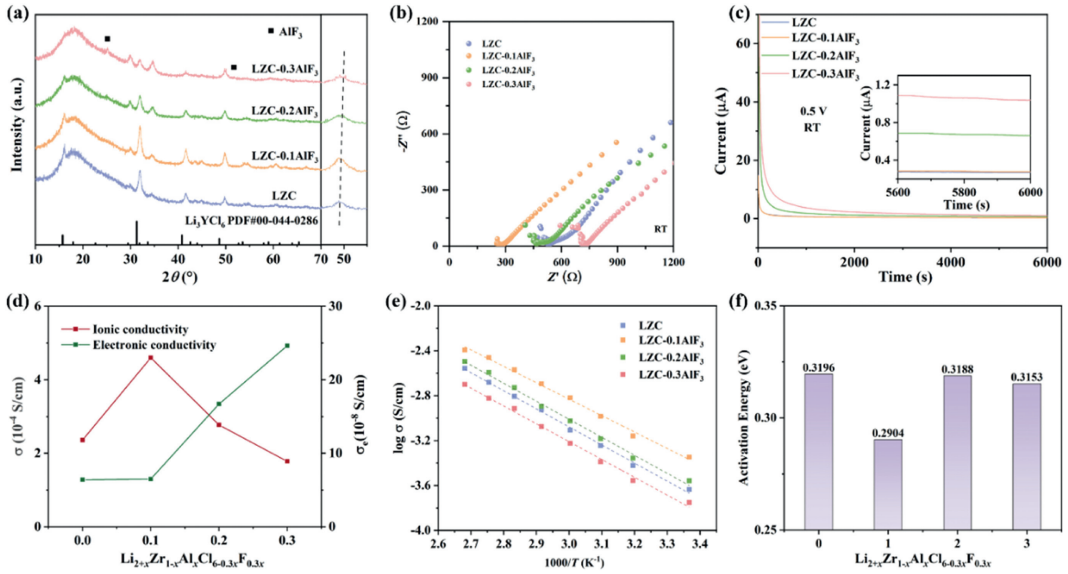

Fig. 1. (a) XRD patterns, (b) Nyquist impedance plots, (c) DC polarization current, (d) room-temperature ionic and electronic conductivity, (e) Arrhenius conductivity plots and, (f) activation energy of the $Li_{2+x}Zr_{1-x}Al_xCl_{6-3x}F_{3x}$ ($x = 0$, 0.1, 0.2 and 0.3) SEs.

disorder [24]. In the case of sulfide SEs, Zhang *et al*. found that MoS_4^{4-} preferentially replaces $P_2S_7^{-}$ in $Li_7P_3S_{11}$, thereby widening the Li^+ pathway, forming Li vacancies, and promoting ion conduction [25]. For halide SEs, Yu *et al*. used Y^{3+} doping to enhance the ionic conductivity of Li_2ZrCl_6 [26]. Additionally, cation doping may form Li-alloys at the anode side and enhances anodic interface stability. Al doping on Li-argyrodites can improve the ionic conductivity [27], while the Al doping on Li_3PS_4 can improve the Li dendrite suppression capability [28]. Yang *et al*. demonstrated that Li-Al alloys formed at the SE/Li interface can inhibit the growth of Li dendrites during cycling [28]. Lin *et al*. also suggested that Li-Zn alloy has high chemical resistance, and thus reduces side reactions between the Li metal and electrolyte, and contributes to the formation of a stable interface on the Li metal anode [29].

In addition to improve the ionic conductivity, many works reveal that SEs with anion doping may also construct a more stable solid electrolyte interface (SEI) a broadened electrochemical window, which are favorable for a good compatibility to Li electrode and high voltage cathode. A stable SEI with electrically insulating and ionic conducting features enables batteries with a high Coulombic efficiency and good cycling stability [30–33]. Sun *et al*. demonstrated that fluoride sulfide SEs can form an ultra-stable LiF SEI [34]. Wu *et al*. improved the interface compatibility between SE and the Li anode by Cu-Cl co-doping [35]. Sun *et al*. showed that F doping on Li_3InCl_6 can significantly expand its electrochemical window, enabling high-voltage ASSLBs to exhibit good cycling performance [36]. Based on previous studies, it is reasonable to consider Al-F co-doping for improving the overall performance of electrolyte materials, including the compatibility of SEs on both cathode and anode sides.

In this study, we synthesized Al-F dual-doped LZC Li-halides, according to the co-doping strategy. In addition to improve the ionic conductivity, the oxidation window widens from 3.61 V to 4.04 V (*vs*. Li^+/Li, the voltages mentioned below are *vs*. Li^+/Li) by Al-F co-doping. The side-reaction of the cathode is significantly suppressed in the assembled battery run at 3.0–5.1 V. Moreover, a tight contact is observed between the Al-F-doped LZC and active material in the cathode. Notably, a thin Li-Al alloy interface layer is discovered at the surface of Li anode during electrochemical cycling. The Al-F co-doing exhibits significantly enhanced electrochemical properties for LZC-based ASSLBs. It is noteworthy that the Al-F co-doping is also applicable to Li-argyrodite SEs with similar merit and scenario. The prototype of ASSLBs composed of the double electrolyte layers, by combining the Al-F-doped LZC and Al-F-doped Li-argyrodite, demonstrates excellent Li dendrite suppression capability and electrolyte/electrodes interface compatibility. Al-F co-doping is suitable for both halide and sulfide electrolyte materials.

$Li_{2+x}Zr_{1-x}Al_xCl_{6-3x}F_{3x}$ ($x = 0$, 0.1, 0.2 and 0.3) were synthesized by high-energy ball milling method using LiCl, $ZrCl_4$ and AlF_3 raw materials. The samples are designated as LZC, LZC-0.1AlF_3, LZC-0.2AlF_3 and LZC-0.3AlF_3, respectively, according to x values. The X-ray diffraction (XRD) patterns (Fig. 1a) of the as-synthesized $Li_{2+x}Zr_{1-x}Al_xCl_{6-3x}F_{3x}$ samples are assigned to the structure of Li_3YCl_6 with P3_m1 symmetry [37,38]. The peak at 17° is due to the polyimide film used to insulate the air. It can be seen from the XRD patterns that the diffraction peaks shift to a higher angle range with the increase of Al-F doping amount. This indicates a gradual contraction of the $Li_{2+x}Zr_{1-x}Al_xCl_{6-3x}F_{3x}$ unit cell because the ionic radii of Al^{3+} and F^- are smaller than those of Zr^{4+} and Cl^-, respectively. Doping Al^{3+} at the Zr^{4+} site and F^- at the Cl^- site lead to reduction of the crystal lattice. When the doping concentration over $x > 0.2$, the AlF_3 impurity peaks appear, indicating a saturation of doping amount. Fig. S1 (Supporting information) shows the SEM morphology of the LZC-0.1AlF_3 particle. Energy-dispersive spectroscopy (EDS) mapping demonstrates uniform distribution of all elements. These results indicate successful Al-F doping for $Li_{2+x}Zr_{1-x}Al_xCl_{6-3x}F_{3x}$.

A SE should include high lithium-ion conductivity and low electronic conductivity. The ionic conductivity of the as-synthesized $Li_{2+x}Zr_{1-x}Al_xCl_{6-3x}F_{3x}$ ($x = 0$, 0.1, 0.2 and 0.3) samples were tested using the electrochemical impedance spectroscopy (EIS), as shown in Fig. 1b. With the increase of the doping amount, the resistance decreases first and then increases. The minimum impedance is 270 Ω for $x = 0.1$, a much smaller value compared with LZC (535 Ω). The corresponding room temperature ionic conductivities were calculated according to the intersection of the high frequency region of the impedance spectrum at the x-axis. The calculated ionic conductivity (Fig. 1d) of LZC is only 0.24 mS/cm, while that of LZC-0.1AlF_3 is 0.46 mS/cm. The main reason for the increase of ionic conductivity is substitution of Al^{3+} on Zr^{4+}. Previous studies have shown that doping M^{3+} on LZC by trivalent metal elements is ben-

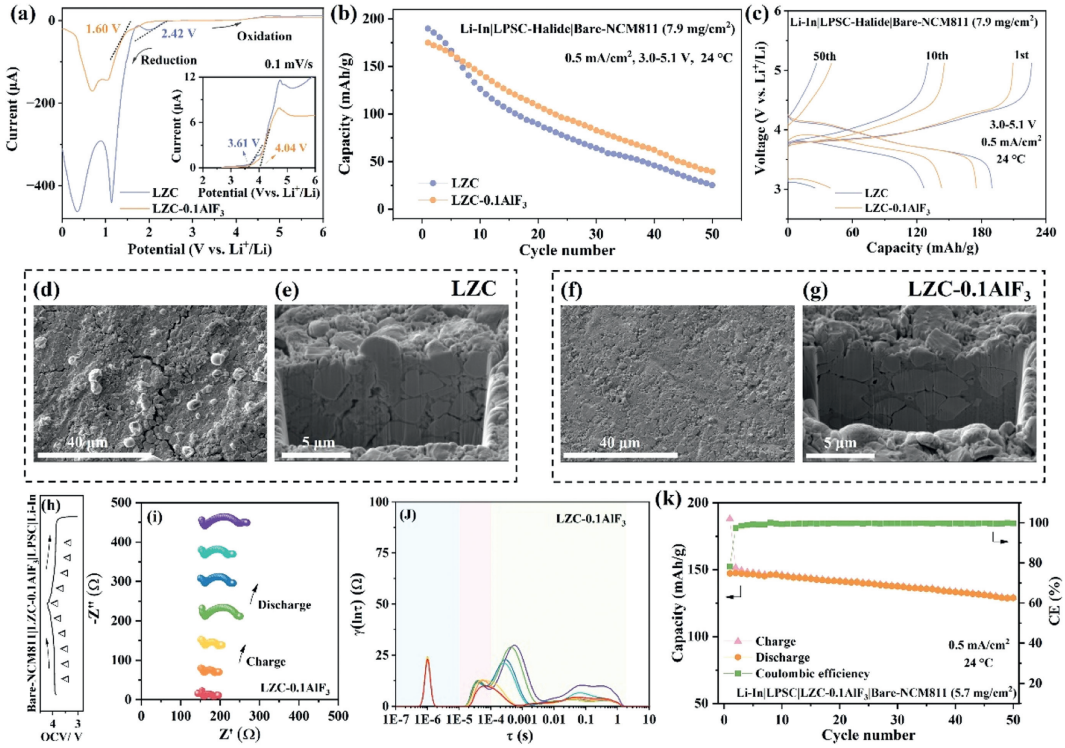

Fig. 2. (a) Cyclic voltammetry profiles of the LZC and LZC-0.1AlF_3 SEs. (b) Cycling performance and (c) charge/discharge profiles of the Li-In|LPSC-halide|bare-NCM811 batteries using LZC and LZC-0.1AlF_3 halide SEs working at 3.0–5.1 V. SEM surface and FIB morphologies of the cathode for (d, e) LZC and (f, g) LZC-0.1AlF_3 batteries after cycling. Impedance evolution of Li-In|LPSC|LZC-0.1AlF_3|bare-NCM811 during the initial charge/discharge stages: (h) Time–voltage profiles. (i) GEIS evolution. (j) DRT transformation obtained from the GEIS curves. (k) Cycling properties of the LZC-0.1AlF_3 battery run at 3.0–4.3 V.

eficial for improving the ionic conductivity. This is mainly due to the expansion of the anisotropic lattice volume and the increase of Li^+ concentration in the (002) plane, which promote Li^+ migration in the microcrystalline structure [39]. The decrease of the ionic conductivity for $x \geq 0.2$ is due to the existence of impurities and a further increase of F concentration in LZC. Li-F is shorter and stronger than Li-Cl bonding, which can lead to local distortions in the Li coordination environment, and thus increases the barrier of Li^+ migration and impedes Li^+ mobility [40]. At room temperature, the electronic conductivity (Figs. 1c and d) of LZC-0.1AlF_3 is 6.5×10^{-8} S/cm, which is comparable to LZC (6.4×10^{-8} S/cm). However, the electronic conductivity increases when $x > 0.1$. This could be due to the formation of Al-based halide impurities due to the excessive Al-F doping. The impurities distributed on the grain boundary and the matrix can increases the electronic conductivity of the samples [41].The variation of ionic conductivity upon temperature conforms to the relationship of activation energy for $Li_{2+x}Zr_{1-x}Al_xCl_{6-3x}F_{3x}$ (Figs. 1e and f). The activation energy of LZC-0.1AlF_3 is 0.2904 eV, which is the lowest value in these samples. Therefore, moderate Al-F doping on LZC is favorable for the ion transport.

The electrochemical window was evaluated through cyclic voltammogram (CV) on an asymmetric cell, which consists the mixture of LZC or LZC-0.1AlF_3 with VGCF as cathode, LZC or LZC-0.1AlF_3 as electrolyte, and Li-In anode. The addition of VGCF can improve the reaction rate on the cathode and augments the current signal for detection. At a scan rate of 0.1 mV/s, the cells were subjected to a positive scan and then a negative scan. The oxidation and reduction windows were obtained sequentially to assess the redox stability. As displayed in Fig. 2a, the obtained reduction and oxidation potentials for LZC-0.1AlF_3 are 1.60 and 4.04 V, respectively, which are considerably higher than those of LZC (2.42 and 3.61 V). This indicates that LZC-0.1AlF_3 SE with Al-F doping allows the ASSLBs to operate within a wider electrochemical window. It has been reported that an F-doped electrolytes possess better redox stability, which is originated from the relatively high electronegativity of F [36,42,43].

Since the doping AlF_3 was conducive to improve the oxidation window of LZC, we assembled ASSLBs with double electrolyte layer using LZC (or LZC-0.1AlF_3) paired with a LPSC electrolyte, and using uncoated NCM811 cathode (bare-NCM811 mixed with LZC or LZC-0.1AlF_3) and Li-In anode. The batteries were cycled at 24 °C in a voltage cut off range of 3.0–5.1 V and a current density of 0.5 mA/cm^2. The discharge capacity during cycling and the selected charge-discharge curves are shown in Figs. 2b and c, respectively. For the LZC-0.1AlF_3 battery, the initial discharge capacity is 175.1 mAh/g and the Coulomb efficiency is 83.68%. The discharge capacities in the first few cycles are lower than those of the LZC battery, which has initial discharge capacity of 189.8 mAh/g (a Coulombic efficiency of 83.72%). However, the LZC-0.1AlF_3 battery shows a better capacity retention (23% at 50 cycles) than the LZC battery (13% at 50 cycles), demonstrating that the Al-F doping is beneficial for the batteries operating at a higher voltage. In addition to F, the incorporation of Al also plays a crucial role on widening the electrochemical window. Numerous studies have demonstrated that doping Al into oxide cathodes significantly enhances their cycling performance at high voltages [44,45]. Therefore, the Al-F co-doping is suitable to improve the upper limit of electrochemical stability for SEs. It should be noted that the capacity decay is mainly attributed to the irreversible damage of the cathode at too high voltages. Fig. S2 (Supporting information) shows the dQ/dV curves of the batteries for the first two cycles. These curves demonstrate irreversible and detrimental damages to NCM811 when charging to the voltage of 5.1 V, beyond its typical operating voltage at 4.3 V.

Inside the cathode, the most significant mechanical challenge arises from the volume changes experienced during charging and

discharging [46,47]. A volume contraction due to the formation of gaps between the active material and electrolyte particles leads to contact loss, which occurs because SEs are unable to flow and cannot a maintain good contact with the particles of the active material during volume variation. The formation of voids causes ion blocking, so the contact loss leads to the decrease in cathode utilization and to the high impedance, and finally causes battery failure [48]. To investigate the contact between LZC-0.1AlF_3 and the active material, the cycled batteries were detached and subjected to chemical and microstructural characterizations. SEM images detected on the cathode surface of the LZC battery (Fig. 2d) show bits pores and long cracks, which would hinder the Li^+ diffusion and block the charge transfer [49,50]. In contrast, the cathode surface of the LZC-0.1AlF_3 battery (Fig. 2f) demonstrates a much denser microstructure without long cracks. The microstructure of the composite cathode was further investigated using FIB for an intuitive view inside the cathode (Figs. 2e and g). Even after 50 cycles at 5.1 V, LZC-0.1AlF_3 maintains good contacts with NCM811 particles, without significant voids or cracks. However, obvious contact losses are observed inside the cathode for the battery using LZC. This reveals that the Al-F doping on LZC is conducive to maintain the cathode microstructure. This advantage is ascribed to the enhanced electrochemical stability of LZC-0.1AlF_3 at high voltage in contrast to LZC, thus the decomposition of the former is less than that of the latter.

The interface performance in the cathode was further evaluated by the impedance spectroscopy. Figs. 2h-j and Fig. S3 (Supporting information) show the initial charge-discharge curves and the corresponding in-situ EISs of LZC and LZC-0.1AlF_3 ASSLBs, respectively. In the whole cycle, the resistance growth of the LZC battery is significantly higher than that of LZC-0.1AlF_3 battery. To decouple the contribution of each part on resistance increasement, the distribution of relaxation times (DRT), a semi-quantitative method, was employed to analyze the impedance spectra (Fig. 2j and Fig. S3c). The spectra are divided into three parts based on their relaxation times. The high frequency part (marked in blue) corresponds to grain boundary response in the SE. The pink region reflects the transport of Li^+ in the anodic interface between SE and Li-In electrode (SEI layer). The green area is related to represent the charge transfer processes [51–54]. Comparing the curves of the LZC battery and LZC-0.1$AllF_3$ battery, it can be observed that the peak value change in the pink region primarily originates from the interface between LPSC and Li-In, which is attributed to the utilization of sandwich LPSC on the anode side in this study. In the green area, the peak intensity changes in the LZC-0.1AlF_3 battery are relatively small (less than that of the LZC battery), indicating that the battery exhibits superior cathode electrochemical stability during the charge and discharge process.

When adjusting the upper limit voltage from 5.1 V to 4.3 V (a voltage commonly used in literature), the Li-In|LPSC-LZC-0.1AlF_3|Bare-NCM811 battery shows decent cycling stability at the current density of 0.5 mA/cm^2 (Fig. 2k and Fig. S4 in Supporting information). The discharge capacity at the 1st cycle is 147.2 mAh/g. The capacity retention rate is 87.5% after 50 cycles.

To investigate the influence of the Al-F co-doping on the chemical stability of LZC toward Li, the EIS tests were conducted on the Li||Li symmetrical setup using LZC and LZC-0.1AlF_3 SEs (Fig. S5 in Supporting information). The impedance of Li|LZC|Li significantly grows with increasing time. The corresponding resistance increases to ~225 kΩ at 200 h. In sharp contrast, the Li|LZC-0.1AlF_3|Li cell demonstrates an increased resistance only at the initial state, and then stabilizes at ~2 kΩ after 200 h. This may be attributed to the formation of advantageous interphases between Li and LZC-0.1AlF_3, which retard the continuous side-reaction at the interface region.

To evaluate the kinetic stability of AlF_3-doped LZC against Li, CV experiments were conducted on the Li|SE|Steel cells, scanned in a voltage range of −0.5 V to 5 V at a scan rate of 0.1 mV/s (Figs. 3a and b). Compared with the AlF_3-doped LZC, the overlap of the LZC curves is poor during both the cathodic and the anodic scans, demonstrating significant current fluctuation. This confirms that the Al-F co-doping improve the electrochemical stability of LZC during the Li^+ plating and stripping processes. Moreover, the Al-F co-doping effectively is beneficial for inhibiting the growth of lithium dendrites. As depicted in Fig. 3c, the CCD of the Li|LZC-0.1AlF_3|Li symmetric cell is 1.4 mA/cm^2 (tested at a step-increased current density of 0.1 mA/cm^2). Fig. 3d displays the long-term Li plating/stripping test on Li||Li symmetric cells using LZC, LZC-0.1AlF_3, and LZC-0.2AlF_3 SEs, at the current density of 0.1 mA/cm^2 at room temperature. The plating/stripping potential of the LZC symmetric cell rapidly increases to 5 V, reaching the overlimit of the apparatus. The fluctuant voltage indicates an unstable interface and/or soft short-circuits. However, the LZC-0.2AlF_3 cell is much better. Its polarization voltage steady increases and finally reaches 5 V at about 300 h. In sharp contrast, the LZC-0.1AlF_3 symmetric cell exhibits significantly improved cycling stability for over 360 h, only with a slow increase in polarization voltage compared to the other two symmetric cells. It is worth noting that the polarization voltage increases mainly within the first 100 h, and after that, the interface resistance remains nearly unchanged.

The cycled LZC and LZC-0.1AlF_3 symmetric cells were detached for microstructural/chemical detection on the interface region. The SEM and EDS spectra of the cross-section are displayed in Figs. 3e and f. There is a noticeable gap between Li and LZC SE (Fig. 3e), which may seriously affect the Li^+ transport. From the EDS mappings, it can be clearly seen that a Cl-rich interface layer forms after cycling. In comparison, the interface of the LZC-0.1AlF_3 cell does not have such a gap layer. The Zr content at the interface for the LZC-0.1AlF_3 cell is much higher than the LZC cell. The different interfacial morphologies and elemental distributions cause the different cycling behaviors and polarization voltages in the LZC and LZC-0.1AlF_3 symmetric cells (Fig. 3d). The generation of interfacial products does not lead to short-circuits or continuous reactions, but rather reaches a dynamically stable state and a robust interface. In addition, it is interesting to reveal that a thin Li-Al alloy layer is observed on the surface of the Li-metal electrode for the LZC-0.1AlF_3 cell. The Al ions migrate to the anode side and form a solid solution with Li metal, thereby facilitating uniform lithium plating [55]. This Li-alloy layer is conductive to stabilize the polarization during the Li^+ plating/stripping process. The generation of Li-Al alloy can effectively reduce the charge transfer resistance, improve the cycle stability, and increase the Coulombic efficiency in lithium batteries [56,57]. Therefore, LZC-0.1AlF_3 exhibits good electrochemical stability against Li.

To further evaluate the interfaces and interphases, X-ray photoelectron spectroscopy (XPS) was conducted on the original samples and the interfacial layers (with black color) detached from the cycled Li||Li symmetric cells (Fig. 4). Figs. 4a and b depict the interface of LZC cell and the comparison with the as-synthesized LZC sample. After Li plating/stripping cycling, the corresponding peaks changes obviously, indicating the presence of new components at the interface in addition to the pristine ones. The main decomposition products for LZC cell contain Li-Cl and Zr-Cl after cycling. The data before and after cycling are in good agreement with those reported previously [39,58]. However, the scenario is rather different observed from the LZC-0.1AlF_3 cell (Figs. 4c and d). Li 1s spectra (Fig. 4d) reveal the existence of Li-F and Li-Al interphases in addition to Li-Cl. Zr 3d spectra show Zr-F in addition to Zr-Cl signals. More important, both Li 1s and Zr 3d spectra demonstrate that the amount of the decomposed products of LZC-0.1AlF_3 is significantly lower than those of LZC cell; the major part of the LZC-0.1AlF_3 SE remains intact after cycling. The fitting of F 1s and Al 2p spectra confirm the formation of Li-F and Li-Al compounds at the interface

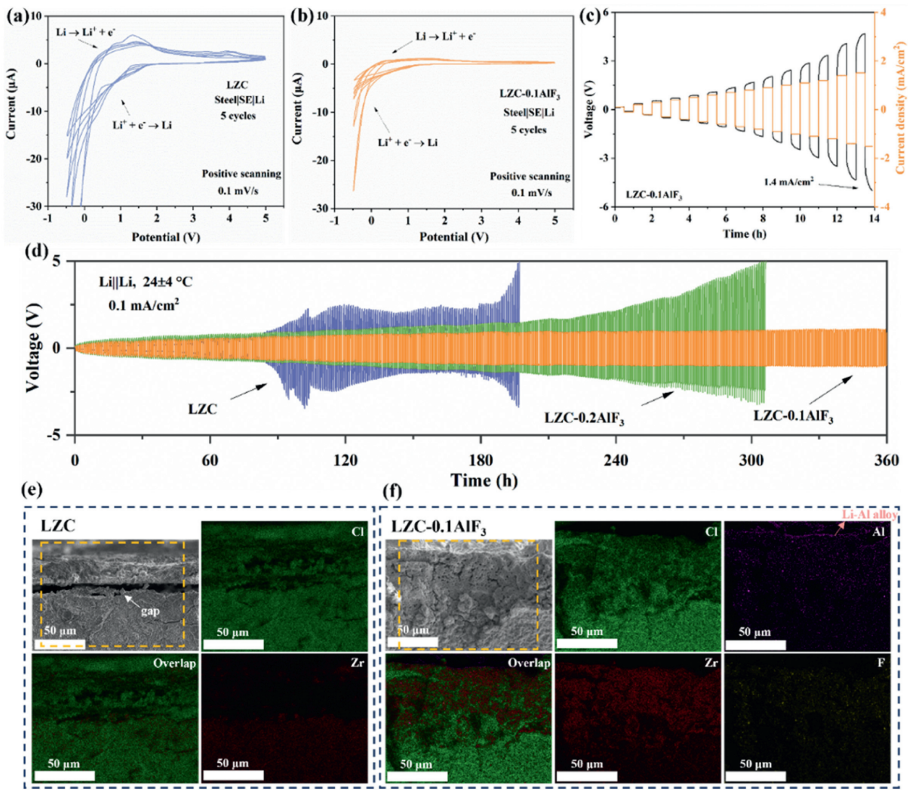

Fig. 3. CV tests of the assembled Li|SEs|steel asymmetric cells using (a) LZC and (b) LZC-0.1AlF_3 SEs. (c) CCD evaluation for the LZC-0.1AlF_3 symmetric cell. (d) Galvanostatic cycling profiles for the cells using the LZC, LZC-0.1AlF_3, and LZC-0.2AlF_3 SEs at 0.1 mA/cm^2. SEM-EDS analysis at the Li/SE interface for the Li||Li cells after cycling using (e) LZC and (f) LZC-0.1AlF_3 SEs.

region [6,28]. The appearance of diverse characteristic peaks is the evidence of Li/SE interfacial evolution during Li plating/stripping.

Mechanism for enhancing the kinetic stability of the Li/halides interface by Al-F co-doping is proposed as follows (Fig. 4e). At the LZC/Li interface, cracks exist between electrolyte and Li electrode during cycling, resulting in a poor contact. Additionally, the Li-Cl and Zr-Cl interphases are not sufficient to suppress the Li/halide interface reactions for a long period. Accumulation of reaction products causes an increase in interface resistance, hindering the Li^+ migration. By contrast, the reaction products formed at the interface of LZC-0.1AlF_3/Li contain fluorides such as Li-F and Zr-F, which are favorable for constructing a robust interface layer and maintaining stable interphases toward advanced batteries. In addition, the interphases may partially fill the voids/gaps at the interface [59]. Consequently, the electrochemical stability of halide/Li is significantly enhanced.

The potential application of LZC-0.1AlF_3 SE in ASSLBs was evaluated through assembling Li||Bare-LCO battery using uncoated LCO mixed with LZC-0.1AlF_3 as a composite cathode and LZC-0.1AlF_3 as electrolyte, and compared with the battery using LZC (Fig. S6 in Supporting information). At a current density of 0.1 mA/cm^2, the initial discharge capacity of LZC and LZC-0.1AlF_3 batteries show comparable value of 120.4 and 124.6 mAh/g, respectively. However, after the following five cycles, the capacity retention rate of LZC drops to only 66%, while that of LZC-0.1AlF_3 is 76%, demonstrating improved cycling stability by Al-F co-doping. The capacity decay is mainly induced by the interface reaction between SE and Li electrode [59]. These two batteries were disassembled and performed XRD measurement at the interface region. As shown in Fig. S7 (Supporting information), LZC shows almost amorphous characteristics without LZC diffraction peaks, indicating a complete LZC/Li reaction at the interface region. By contrast, the LZC-0.1 AlF_3 battery still remains part of original LZC-0.1 AlF_3 electrolyte. This result further confirms that the Al-F co-doping improves the (electro)chemical stability of Li/SE. By substituting the Li metal with Li-In alloy, the cycling stability is significantly improved for the LZC-0.1AlF_3 battery. As shown in Fig. S8 (Supporting information), the Li-In|LZC-0.1AlF_3|LCO cell exhibits initial discharge capacity of 133.8 mAh/g (with a Coulombic efficiency of 93%) and a decent capacity retention rate, much better than the LZC battery. This result further confirms the benefit of Al-F co-doping towards halide/Li compatibility.

To validate the universality of Al-F co-doping effect on other types of SEs, we synthesized Cl-rich Li-argyrodites with different Al-F doping contents, *i.e.*, $Li_{5.7-x}P_{1-x}Al_xS_{4.7-3x}Cl_{1.3}F_{3x}$ ($x = 0$, 0.03, 0.05, 0.07, 0.1, and 0.15). The samples are sequentially designated as Cl13–0, Cl13–003, Cl13–005, Cl13–007, Cl13–010, and Cl13–015, respectively. The XRD (Fig. S9 in Supporting information) profiles show that the crystal structure of all samples is assigned to the argyrodite-type cubic structure ($F\bar{4}3m$). LiF and $Li_8P_2S_9$ impurity phases appear in the samples for $x \geq 0.1$. With increasing Al-F doping amount, the characteristic peaks of the main phase slightly shift to lower angles, indicating a successful substitution of P atoms (with a smaller ionic radius) by Al atoms in the lattice, leading to a lattice expansion [27]. Fig. S10 (Supporting information) displays the Nyquist plots tested at room temperature for $Li_{5.7-x}P_{1-x}Al_xS_{4.7-3x}Cl_{1.3}F_{3x}$. The impedances only show a negligible change upon Al-F doping. The room temperature ionic conductivity is 4.15 mS/cm for Cl13–0 and is 4.04 mS/cm for Cl13–007. Thus, the Al-F co-doping does not deteriorate the ion transport performance. The CCDs for $Li_{5.7-x}P_{1-x}Al_xS_{4.7-3x}Cl_{1.3}F_{3x}$ with selected x are shown in Fig. 5a and Fig. S11 (Supporting information). The value is only 1.0 mA/cm^2 for Cl13–0 (Fig. S11), while Cl13–007 can reach up to 1.7 mA/cm^2. Fig. 5b shows the long-term Li

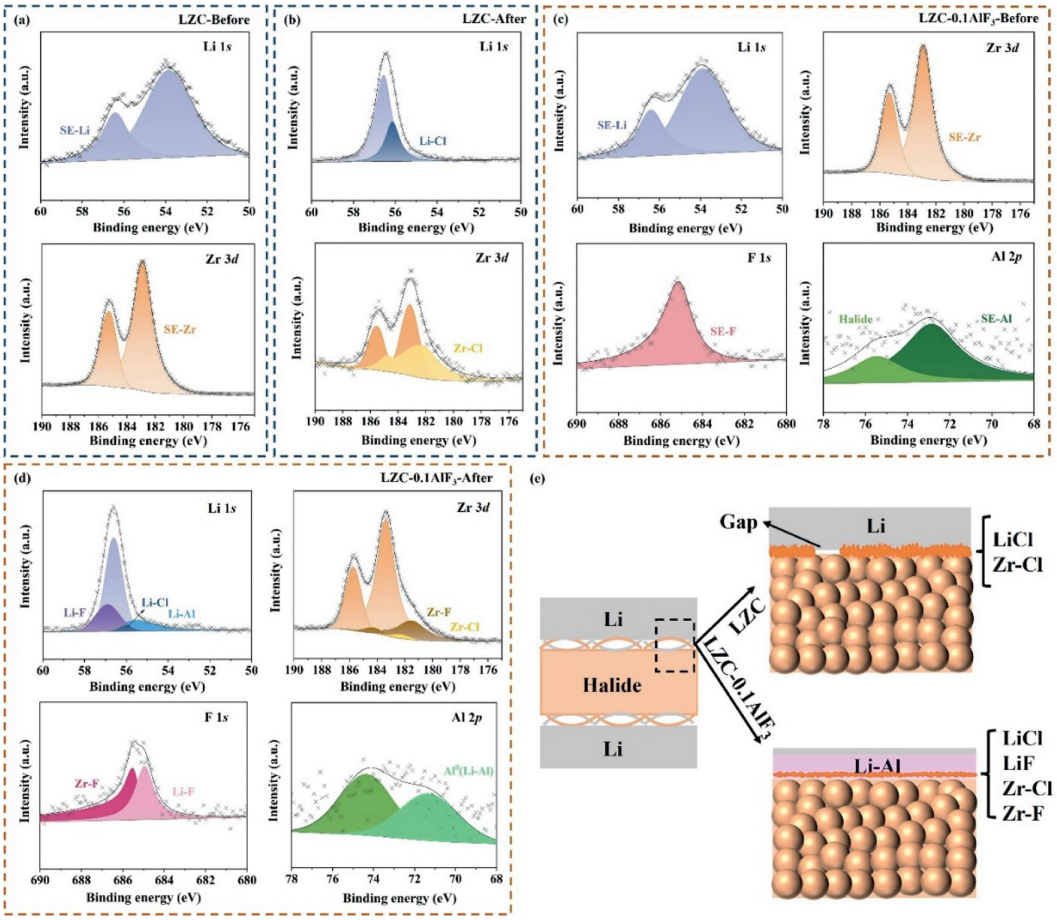

Fig. 4. XPS evaluation on the intact SEs and the Li/SE interface on the Li||Li cells after cycling: (a) Pristine and (b) cycled LZC cell. (c) Pristine and (d) cycled LZC-0.1AlF_3 cell. (e) Schematic diagram illustrating the effect of Al-F co-doping on the Li/SE interface.

plating/stripping on a Li|Cl13–007|Li symmetric cell at 0.5 mA/cm^2. The cell can well cycle for more than 2000 h. The Li||Li symmetric cells with Cl13–0 and Cl13–007 SEs were also assembled respectively and cycled at a current density of 0.1 mA/cm^2 to compare the polarization voltage (Fig. S12 in Supporting information). Comparing the voltage profiles, the cell using Cl13–007 demonstrates low polarization voltages than Cl13–0 SE. The voltage-increase for Cl13–007 is 3 mV, whereas for Cl13 is over 5 mV. The Li|Cl13–007|Li cell can run over 30 cycles (Fig. S13 in Supporting information) without short circuits at a current density of 1 mA/cm^2, whereas the Li|Cl13|Li cell suffers "hard" short circuits less than 4 cycles [22]. These results suggest that the Cl13–007 SE possesses better long-term cycling stability and dendrite suppression capability compared with the Cl13–0 SE [23,60]. The SEM-EDS images collected on the cross-section of the interface are shown in Fig. S14 (Supporting information). At the Li/Cl13–007 interface, a Cl-rich layer mainly composed of LiCl interphase was detected. Previous studies have suggested that a LiCl-dominated SEI layer for sulfide SEs is conducive, serving as a buffering layer to stabilize the interface between Li and sulfide. Notably, a Li-Al alloy layer was observed on the Li surface of the Cl13–007 cell, which would play a role on manipulating uniform Li depositions during Li^+ plating/stripping. This scenario is consistent with the behavior observed in LZC-0.1AlF_3 above-mentioned. It is worth noting that the Li|Cl13–007|LZC-0.1AlF_3|Cl13–007|Li symmetric cell, using the SE combining LZC-0.1AlF_3 with Cl13–007, exhibits a high CCD of 3 mA/cm^2 (Fig. 5c). When subjected to a long-term galvanostatic cycling under a high current density of 1 mA/cm^2, the symmetric cell can well work more than 300 cycles with high cycling stability without short-circuits (Fig. 5d). This result indicates that a double-layer SE system with the combination of halide/sulfide is effective to suppress Li dendrites and enhance the electrochemical cycling performance. The primary reason for the enhanced performance of the bilayer electrolyte origins from sandwiching a less stable electrolyte between more stable electrolytes. This setup facilitates localized decomposition in the unstable electrolyte layer (LZC-0.1AlF_3 in this work), thereby preventing the growth of lithium dendrites [50,61].

The as-synthesized Cl13–0 and Cl13–007 SEs, Li_2O-coated $LiCoO_2$ (LO@LCO), and Li metal were then used to assemble the ASSLBs. Figs. 5e and f show the cyclic performance of Li||LO@LCO at the current density of 0.1 mA/cm^2. The performance of the Cl13–007 battery significantly outperforms the Cl13–0 battery. The former shows initial discharge capacity of 122.0 mAh/g and a capacity retention rate of 84.3% after 50 cycles, while the latter experiences a rapid capacity decrease at first few cycles and only maintains a retention rate of 65.7% after 50 cycles. Moreover, the initial Coulombic efficiency (Fig. 5e) of Cl13–0 is 77.1% and is lower than Cl13–007 (85.0%). The reasons for the inferior initial Coulombic efficiency for Cl13 can be attributed to two aspects [62–64]. First, the stability of Cl13 towards active materials is lower than that of Cl13–007, because the Al-F co-doping effectively suppresses (electro)chemical reactions in the cathode. Second, Cl13 is less stable against metallic Li than Cl13–007. This result further illustrates the excellent interface compatibility between the Al-F-doped argyrodites and Li metal. We subsequently performed SEM characterization on the cathode surface of the cycled batteries (Fig. S15 in Supporting information). The Cl13–0 battery (Fig. S15a) shows

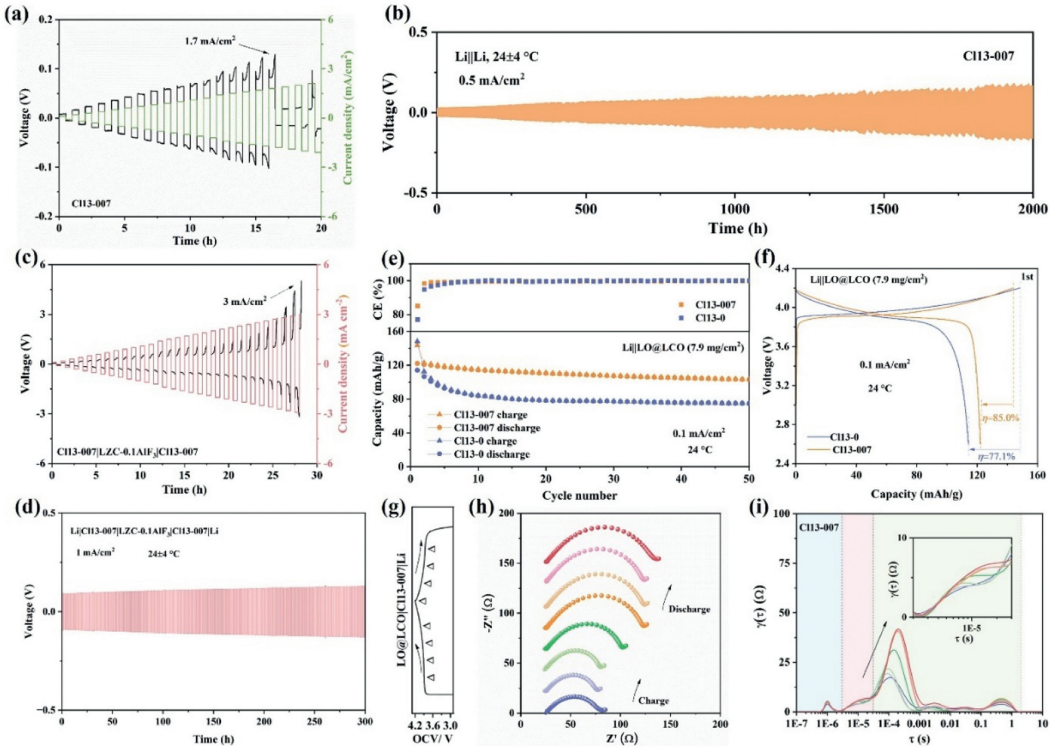

Fig. 5. (a) CCD evaluation and (b) galvanostatic cycling curve for the Li||Li symmetric cell. (c) CCD evaluation and (d) long-term galvanostatic cycling on a Li|Cl13–007|LZC-0.1AlF_3|Cl13–007|Li symmetric cell. (e) Galvanostatic cycling performance and (f) corresponding initial charge/discharge profiles of Li||LO@LCO batteries using Cl13–0 and Cl13–007 SEs. Impedance evolution of Li||LO@LCO batteries using Cl13–007 SEs: (g) Time–voltage profiles. (h) GEIS evolution. (i) DRT transformation obtained from GEIS.

more cracks and pores between active material and catholyte than the Cl13–007 battery (Fig. S15b), indicating that the latter is superior to the former as a catholyte.

The Li electrode was peeled off carefully and observed the morphology with SEM for the Li||LO@LCO batteries using Cl13–007 and Cl13–0 SEs after cycling. Due to the tight contact between the electrolyte and Li electrode by forming interphases, a complete separation is difficult. As shown in Fig. S16 (Supporting information), no obvious Li dendrite is observed on the surface. However, compared with the Cl13–007 battery (Fig. S16a), it is apparent that the Cl13–0 battery (Fig. S16b) forms a rougher morphology and shows cracks, which are prone to induce Li dendrite growth [65]. This observation indicates that Cl13–007 outperforms Cl13–0 SE on suppressing Li dendrite growth.

The EIS-DRT analyses were performed on the Li||LO@LCO batteries using Cl13–0 and Cl13–007 Ses (Figs. 5g-i and Fig. S17 in Supporting information). The peak intensity of Cl13–007 in the pink area (related to the Li^+ transport at the anode side) is smaller than that of Cl13–0 (insets of Fig. 5i and Fig. S17c), further confirming the improved interface stability of Li|argyrodite by Al-F co-doping.

In summary, the influences of Al-F co-doping on the physicochemical properties of Li-halide systems were systematically investigated using as-synthesized $Li_{2+x}Zr_{1-x}Al_xCl_{6-3x}F_{3x}$ compounds and were further verified in $Li_{5.7-x}P_{1-x}Al_xS_{4.7-3x}Cl_{1.3}F_{3x}$ Li-argyrodites. In the halide series, it revealed that an appropriate Al-F doping concentration widens the electrochemical window by improving the cathode stability at high voltages and the compatibility against Li anode, and meanwhile, enhances the ion conductivity. Moreover, observed from the FIB-SEM images, the composite cathode using LZC-0.1AlF_3 demonstrates a tighter contact than that using LZC after electrochemical cycling, indicating a better compatibility of the former towards active materials. During long-term Li plating/stripping tests, the LZC-0.1AlF_3 SE maintains a stable Li/SE interface, while the LZC SE suffers a high polarization voltage over the upper limit of the apparatus. The poor Li/LZC interface is further evidenced from the SEM-EDS images, where gaps are observed at the interface region. By contrast, a dense interface is observed for Li/LZC-0.1AlF_3, where Li-F and Zr-F were detected. Simultaneously, a thin Li-Al alloy layer is formed on the surface of Li electrode, which along with the fluorides lead to an enhanced compatibility at the Li/SE interface. The similar scenario exhibits in the Li-argyrodite system. The optimized Li-argyrodite (Cl13–007) achieves a higher initial Coulombic efficiency and capacity retention rate than the undoped Li-argyrodite. These results revealed that Al-F co-doping is an effective way approaching high-performance SEs for solid-state batteries.

Declaration of competing interest

The authors declare that they have no known competing financial interests or personal relationships that could have appeared to influence the work reported in this paper.

Acknowledgment

This work was supported by the National Natural Science Foundation of China (Nos. 52172243, 52371215).

Supplementary materials

Supplementary material associated with this article can be found, in the online version, at doi:10.1016/j.cclet.2024.109568.

References

[1] A. Manthiram, X. Yu, S. Wang, Nat. Rev. Mater. 2 (2017) 1–16.
[2] D. Larcher, J.M. Tarascon, Nat. Chem. 7 (2014) 19–29.
[3] J. Janek, W.G. Zeier, Nat. Energy 1 (2016) 1–4.
[4] L.Z. Fan, H. He, C.W. Nan, Nat. Rev. Mater. 6 (2021) 1003–1019.

[5] D.H.S. Tan, A. Banerjee, Z. Chen, Y.S. Meng, Nat. Nanotechnol. 15 (2020) 170–180.
[6] P. Ganesan, M. Soans, M.A. Cambaz, et al., ACS Appl. Mater. Interfaces 15 (2023) 38391–38402.
[7] J. Wang, F. Chen, L. Hu, C. Ma, Nano Lett. 23 (2023) 6081–6087.
[8] X. Li, J. Liang, N. Chen, et al., Angew. Chem. Int. Ed. 58 (2019) 16427–16432.
[9] S. Wang, Q. Bai, A.M. Nolan, et al., Angew. Chem. Int. Ed. 58 (2019) 8039–8043.
[10] A.M. Nolan, Y. Zhu, X. He, et al., Joule 2 (2018) 2016–2046.
[11] B.T. Tham, M.S. Park, J.H. Kim, J. Moon, J. Mater. Chem. A 11 (2023) 15968–15978.
[12] C.H. Wang, J.W. Liang, J. Luo, et al., Sci. Adv. 7 (2021) 9.
[13] H. Kwak, J.S. Kim, D. Han, et al., Nat. Commun. 14 (2023) 2459.
[14] K.B. Hatzell, Matter 5 (2022) 2533–2535.
[15] R. Xu, J. Yao, Z. Zhang, et al., Adv. Sci. 9 (2022) 2204633.
[16] J. Wei, H. Kim, D.C. Lee, et al., J. Power Sources 294 (2015) 494–500.
[17] X. Chen, Z. Guan, F. Chu, et al., InfoMat 4 (2022) e12248.
[18] P. Adeli, J.D. Bazak, K.H. Park, et al., Angew. Chem. Int. Ed. 58 (2019) 8681–8686.
[19] C.H. Wang, J.W. Liang, J.T. Kim, X.L. Sun, Sci. Adv. 8 (2022) 13.
[20] R. Song, J. Yao, R. Xu, et al., Adv. Energy Mater. 13 (2023) 2203631.
[21] C. Wang, S. Wang, X. Liu, et al., Energy Environ. Sci. 16 (2023) 5136–5143.
[22] H. Yan, R. Song, R. Xu, et al., J. Energy Chem. 86 (2023) 499–509.
[23] S. Li, R. Song, R. Xu, et al., J. Alloys Compd. 968 (2023) 172134.
[24] Y. Wang, Y. Wu, Z. Wang, et al., J. Mater. Chem. A 10 (2022) 4517–4532.
[25] Z. Wang, Y. Jiang, J. Wu, et al., Nano Energy 84 (2021) 105906.
[26] S. Chen, C. Yu, C. Wei, et al., Energy Mater. Adv. 4 (2023) 0019.
[27] Y.J. Choi, S.I. Kim, M. Son, et al., Nanomater 12 (2022) 4355.
[28] P. Yu, N. Ahmad, J. Yang, et al., J. Energy Chem. 86 (2023) 382–390.
[29] Y. Lin, Z. Wen, C. Yang, et al., Electrochem. Commun. 108 (2019) 106565.
[30] S. Zhang, B. Cheng, Y. Fang, et al., Chin. Chem. Lett. 33 (2022) 3951–3954.
[31] J. Pan, J. Li, H. Dong, et al., Chem. Eng. J. 447 (2022) 137401.
[32] C. Qiu, Y. Hong, K. Shi, et al., Chem. Eng. Sci. 281 (2023) 119088.
[33] Z. Li, L.P. Hou, X.Q. Zhang, et al., Battery Energy 1 (2022) 20220006.
[34] F. Zhao, Q. Sun, C. Yu, et al., ACS Energy Lett. 5 (2020) 1035–1043.
[35] B.W. Taklu, W.N. Su, Y. Nikodimos, et al., Nano Energy 90 (2021) 106542.
[36] S. Zhang, F. Zhao, S. Wang, et al., Adv. Energy Mater. 11 (2021) 2100836.
[37] K. Wang, Q. Ren, Z. Gu, et al., Nat. Commun. 12 (2021) 4410.
[38] S. Chen, C. Yu, S. Chen, et al., Chin. Chem. Lett. 33 (2022) 4635–4639.
[39] H. Kwak, D. Han, J. Lyoo, et al., Adv. Energy Mater. 11 (2021) 2003190.
[40] W. Tang, W. Xia, F. Hussain, et al., J. Power Sources 568 (2023) 232992.
[41] K. Takahashi, J. Ohmura, D. Im, et al., J. Electrochem. Soc. 159 (2012) A342–A348.
[42] T.W. Yu, J.W. Liang, L. Luo, et al., Adv. Energy Mater. 11 (2021) 9.
[43] J.Y. Huang, K. Iputera, A. Jena, et al., J. Chin. Chem. Soc. 69 (2022) 1233–1241.
[44] M. Xie, T. Hu, L. Yang, Y. Zhou, RSC Adv. 6 (2016) 63250–63255.
[45] C.Z. Zhao, Q. Zhao, X. Liu, et al., Adv. Mater. 32 (2020) 1905629.
[46] J. Gu, Z. Liang, J. Shi, Y. Yang, Adv. Energy Mater. 13 (2022) 2203153.
[47] Y.Bae Song, H. Kwak, W. Cho, et al., Curr. Opin. Solid State Mater. Sci. 26 (2022) 100977.
[48] G. Deysher, P. Ridley, S.Y. Ham, et al., Mater. Today Phys. 24 (2022) 100679.
[49] J. Fu, S. Yang, J. Hou, et al., J. Power Sources 556 (2023) 232465.
[50] H. Zhang, Z. Yu, J. Cheng, et al., Chin. Chem. Lett. 34 (2023) 108228.
[51] D. Qu, W. Ji, H. Qu, Commun. Mater. 3 (2022) 61.
[52] Y. Lu, C.Z. Zhao, R. Zhang, et al., Sci. Adv. 7 (2021) 10.
[53] Y. Lu, C.Z. Zhao, J.Q. Huang, Q. Zhang, Joule 6 (2022) 1172–1198.
[54] L. Li, J. Yao, R. Xu, et al., Energy Stor. Mater. 63 (2023) 108228.
[55] Y.G. Lee, S. Fujiki, C. Jung, et al., Nat. Energy 5 (2020) 299–308.
[56] L. Wang, S. Fu, T. Zhao, et al., J. Mater. Chem. A 8 (2020) 1247–1253.
[57] H. Zhuang, P. Zhao, G. Li, et al., J. Power Sources 455 (2020) 227977.
[58] H. Zhang, Z. Yu, H. Chen, et al., J. Energy Chem. 79 (2023) 348–356.
[59] X. Luo, X. He, H. Su, et al., Chem. Eng. J. 465 (2023) 143036.
[60] T. Chen, D. Zeng, L. Zhang, et al., J. Energy Chem. 59 (2021) 530–537.
[61] L. Ye, X. Li, Nature 593 (2021) 218–222.
[62] Z. Zhang, L. Zhang, X. Yan, et al., J. Power Sources 410-411 (2019) 162–170.
[63] D. Zhang, L. Zhang, K. Yang, et al., ACS Appl. Mater. Interfaces 9 (2017) 36886–36896.
[64] C. Fang, J. Li, M. Zhang, et al., Nature 572 (2019) 511–515.
[65] J. Zhao, C. Zhao, J. Zhu, et al., Nano Lett. 22 (2021) 411–418.